Journal of Materials Chemistry A

ROYAL SOCIETY OF CHEMISTRY

PAPER

View Article Online
View Journal | View Issue

Check for updates

Cite this: *J. Mater. Chem. A*, 2024, **12**, 5225

A 3D nanofiber network anode expediting mass and proton transport to boost proton exchange membrane water electrolysis†

Maolin Geng,[ab] Zhenlan Dou,[e] Hao Zhao,[ab] Qiansen Wang,[ac] Chunyan Zhang,[e] Zhiqing Zou,[ad] Jun Li,*[a] Hui Yang [acd] and Qingqing Cheng *[a]

The key to promote the performance of proton exchange membrane water electrolysis (PEMWE), in addition to the development of high-performance electrocatalysts, lies in how to rationally design and controllably construct nanostructured membrane electrode assembly (MEA) with a maximized triple-phase reaction boundary (TPRB). Herein, a novel 3D nanofiber network (3D-FNT) anode is controllably fabricated *via* electrospinning combined with a nano-transfer strategy. This novel MEA can dramatically lower the IrO_2 loading from 1.0 to 0.1 mg cm^{-2} while ensuring a superior performance (1.737 V@1.5 A cm^{-2}) together with an impressive stability, and outperforms the most reported nanostructured MEAs to date. Electrochemical impedance spectroscopies elucidate that both the 3D network and 1D Nafion channels improve mass transport and proton conduction by 1.34 and 7.76 fold, respectively, compared with the traditional MEA, shedding light on the performance enhancement mechanism. This work paves a way to defuse the cost and performance issues confronting practical PEMWE.

Received 4th November 2023
Accepted 16th January 2024

DOI: 10.1039/d3ta06746g

rsc.li/materials-a

1 Introduction

Proton exchange membrane water electrolysis (PEMWE) is considered the greenest technology for hydrogen production, with the advantages of large current density, high hydrogen purity, and fast response time compared to alkaline water electrolysis.[1–3] Currently, most research studies focus on the rational design and controllable synthesis of high-performance electrocatalysts towards the oxygen evolution reaction (OER)[4,5] and hydrogen evolution reaction (HER).[6,7] Nevertheless, there are rare studies on efficiently transferring the activity of the developed electrocatalysts to membrane electrode assembly (MEA) configuration, which is hard but meaningful for the further practical application of PEMWE.[8,9] Commonly, in contrast to the cathodic catalyst layer where fast HER occurs, the structure of the anodic catalyst layer (ACL) directly determines the performance and lifetime of the entire MEA.[10] Generally, the ACL of the MEA fabricated by the conventional catalyst-coated membrane (CCM) method displays a dense stacked structure that easily results in the low utilization of noble-metal catalysts.[11,12] Meanwhile, the low porosity of the ACL and the tortuous pore channels are not conducive to the efficient transport of H_2O and O_2, causing severe concentration polarization at high current densities and hence the declined MEA performance[13,14] (Fig. 1a). Therefore, the rational design and controlled establishment of the ACL structure to maximize the three-phase reaction boundary (TPRB) are significantly crucial to address the above issues.[15]

The routine solution is to increase the porosity of the ACL by the method of using sacrificialhard templates (MgO, ZnO, *etc.*),[16,17] which has been confirmed to simultaneously resolve the problems in the utilization of electrocatalysts and mass transport. Beyond this, a novel ordered structural MEA is proposed to further promote the performance of the MEA through elaborately ordering the interfaces between the ACL and membrane.[18–21] For example, Park[22] *et al.* constructed an anti-opal structured CL for the anode of PEMWE using the applique transfer method. The resultant MEA exhibits much higher electrolysis performance and lower ohmic/charge-transfer resistances than traditional MEA. Our group[23] recently reported a novel ordered MEA based on an anode with a 3D membrane/ACL interface and gradient tapered arrays by the nano-imprinting method, which not only increases the electrochemically active area but also reduces the overpotential

[a]*Shanghai Advanced Research Institute, Chinese Academy of Sciences, Shanghai, 201210, P. R. China. E-mail: lijun@sari.ac.cn; chengqq@sari.ac.cn*

[b]*University of Chinese Academy of Sciences, Beijing, 100049, P. R. China*

[c]*School of Physical Science and Technology, ShanghaiTech University, Shanghai, 201210, P. R. China*

[d]*Shanghai H-Ray S&T Co., Ltd, Shanghai, 201100, P. R. China*

[e]*State Grid Shanghai Municipal Electric Power Company, Shanghai, 200023, P. R. China*

† Electronic supplementary information (ESI) available. See DOI: https://doi.org/10.1039/d3ta06746g

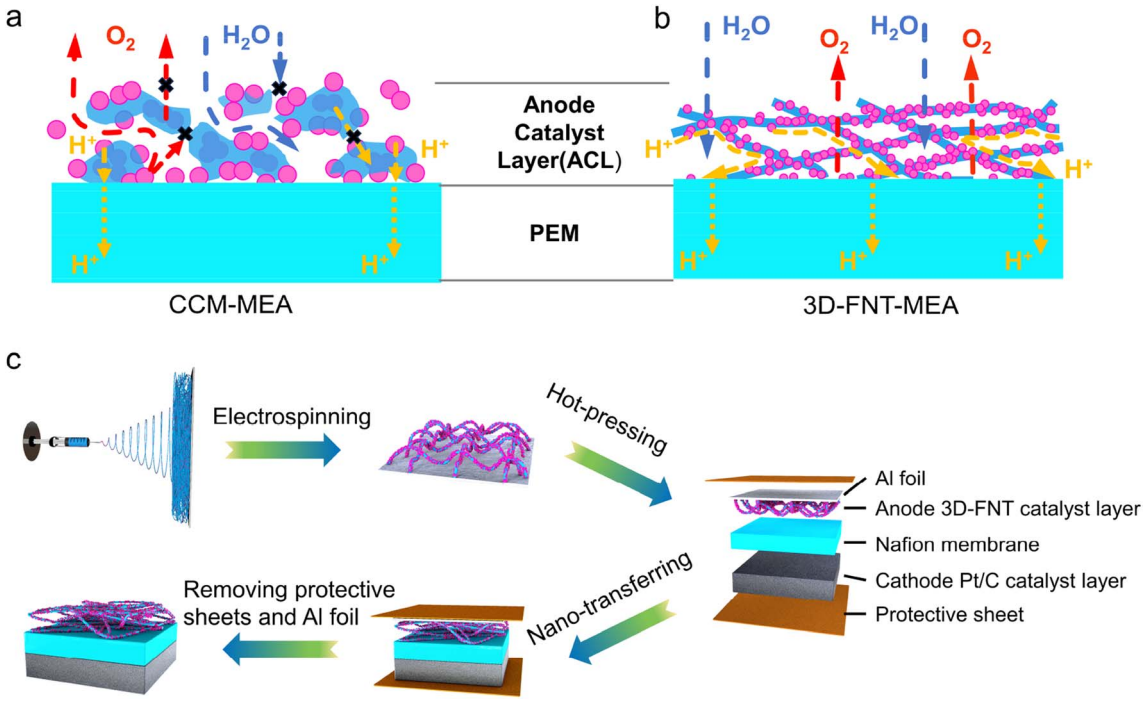

Fig. 1 Schematic illustration of the ACL fabricated by (a) traditional CCM and (b) electrospinning methods. (c) Synthetic procedure for the 3D-FNT-MEA by electrospinning and nano-transferring techniques.

of mass transport and ohmic polarization, realizing a 10-fold reduction in IrO_2 usage. Although great progress has been achieved in the construction of efficient nanostructured MEA, most studies are devoted to expediting the transport of reactants or products, while little attention has been paid to ion transport (*e.g.*, proton (H^+) conduction within the ACL) that is particularly critical for electrocatalysis.[24,25] Generally, the thickness of the actual CL is approximately a few micrometers, the H^+ conduction in the catalyst region adjacent to the membrane relies on the Nafion membrane, while a large proportion of catalyst area away from the membrane is strongly dependent on the ionomer (Nafion resin) for H^+ conduction.[26–28] Nevertheless, the additional ionomer is often difficult to disperse in the CL to build an efficient H^+ conduction channel.[29] At the same time, excessive ionomer content again increases the risk of catalyst embedding, which would impose new problems in catalyst utilization efficiency and mass transport[30] (Fig. 1a). Therefore, how to improve proton transport while ensuring rapid mass transport inside the CL is a formidable challenge.

In this work, we designed and constructed a novel IrO_2/Nafion/PEO 3D nanofiber network (3D-FNT) structure as the ACL of the MEA using electrospinning combined with the nano-transfer strategy. On one hand, the high porosity of this unique 3D-FNT can accelerate water/oxygen transport and improve the exposure of active sites (Fig. 1b). On the other hand, the formed Nafion–PEO composite nanofibers can build a continuous 1D H^+ transport channel, that promote H^+ conduction within the ACL. Electron microscopies verify that the 3D-FNT structure can be controllably constructed by regulating PEO content and metal concentrations. Electrochemical impedance spectroscopy (EIS) corroborates that the H^+ conduction and mass transport impedances of 3D-FNT-MEAs are significantly lower than those of the conventional CCM-MEA, definitely attesting to the superiority of 3D-FNT in the maximum of the TPRB. Notably, the ionomer/catalyst (I/C) ratio can be reduced to 6% while ensuring high H^+ conduction compared to the MEA-CCM with an I/C ratio of 25%. The performance of the optimized 3D-FNT-MEA can reach 1.737 V@1.5 A cm^{-2}, which overwhelms the performance of the CCM-MEA (1.874 V@1.5 A cm^{-2}) at the same IrO_2 loading (0.1 mg cm^{-2}) and is even higher than that of the CCM-MEA with 10-fold IrO_2 loading. Meanwhile, the resultant MEA can maintain over 200 h at a constant current density of 1 A cm^{-2}, indicative of the excellent stability of the 3D-FNT structure.

2 Results and discussion

The fabrication procedure of the 3D-FNT catalyst layer is illustrated in Fig. 1c. Electrospinning was first used to construct the Nafion/PEO/IrO_2 composite nanofiber on alumina (Al) foil. Herein, PEO ($M_w = 600\,000$) is chosen as the additive polymer to adjust the viscosity of precursor solution and plays a critical role in regulating the morphology of the nanofibers. Small irregular aggregates can be observed in the absence of PEO (Fig. S1†), which is attributed to the low viscosity of precursor solution. As the PEO content increases from 1% to 3%, the Nafion/PEO composite nanofiber structure gradually forms with an average diameter of *ca.* 354 nm. It is worth noting that as the PEO content increases to 5% and 7%, the diameter of nanofiber increases, which will cause a decrease in utilization of Nafion

resin on the nanofiber. Therefore, the optimal PEO content is determined to be 3% that can ensure the formation of a suitable composite nanofiber structure.

The content of IrO_2 nanoparticles in the precursor solution is another impact factor that will influence the dispersion of nanoparticles on the Nafion–PEO composite nanofiber. As shown in Fig. S2,† the catalyst nanoparticles cannot be homogeneously dispersed on the nanofibers when the IrO_2 adding content is 20–60 mg. When the IrO_2 content is continued to increase to 80 mg, the surface of nanofibers is almost covered by the uniformly dispersed IrO_2 nanoparticles (Fig. S2d†). However, when the content of IrO_2 further increases to 100 mg, many catalyst agglomerates appear on the nanofibers, indicating that the excessive catalyst is not beneficial for the dispersion of IrO_2 nanoparticles. Based on the above control experiments, the optimal PEO ratio and IrO_2 content were determined to be 3% and 80 mg, respectively. X-ray diffraction (XRD) and X-ray photoelectron spectroscopy (XPS) measurements were performed to analyze the structural variation after the electrospinning process. As shown in Fig. S3,† the electrospun IrO_2 shows an identical crystal structure as well as the chemical state in comparison with the original IrO_2 nanoparticles, definitely demonstrating the unchanged structure for IrO_2, which is the prerequisite for the latter investigation on the effect of the 3D-FNT structure on the MEA performance.

Subsequently, hot-pressing is employed to realize the transfer of the catalyst layer from Al-foil to the Nafion membrane. Compared to the tightly packed structure of the traditional ACL prepared using the CCM (Fig. 2a and b), the novel 3D-FNT ACL displays a nanofiber braided highly porous structure (Fig. 2c and d) with an average nanofiber diameter of *ca.* 435.37 nm (Fig. S4†). Simultaneously, the side-view images (Fig. S5†) also demonstrate that the 3D-FNT ACL (*ca.* 1.67 μm) is thinner than the CCM (3.81 μm), which can expedite the mass transport of water and oxygen. The single nanofiber was further measured by TEM (Fig. 2e and f), indicative of the uniformly distributed IrO_2 nanoparticles on the nanofiber. Notably, the EDS-mapping (Fig. 2g) shows that the F, S, and O elements are well dispersed on the nanofiber, proving the formation of a continuous 1D proton conductor, which can helpreduce the risk of catalyst-embedding by the ionomer. In contrast, the Nafion resin within the CCM ACL is discontinuous (Fig. S6†), which might not be conducive to proton transfer and hence the declined MEA performance.

Prior to measuring the electrolysis performance of the novel MEA, the OER activities for the original IrO_2 nanoparticles and electrospun IrO_2 electrode in a three-electrode system were evaluated to elucidate whether the Nafion nanofiber channel could affect the intrinsic activity of IrO_2 towards the OER. As shown in Fig. S8,† the electrospun IrO_2 electrode (Nafion channel) shows a similar OER activity (335 mV@10 mA cm^{-2}) to that of conventional IrO_2 nanoparticles (329 mV@10 mA cm^{-2}), which implies that the Nafion nanofiber channel cannot improve the OER activity of the IrO_2 catalyst. The MEAs with different ionomer/catalyst (I/C) ratios in the ACL were fabricated to first investigate the effect of the Nafion resin content on the electrolysis performance. FNT-MEAs with I/C ratios of 0, 6, 13, and 21 wt% at IrO_2 a loading of 0.3 mg cm^{-2} are denoted as FNT-MEA-Nafion *X* wt%-0.3 ($X = 0$, 6, 13, and 21%), and the CCM-MEA with the same IrO_2 loading for comparison is denoted as CCM-MEA-0.3. Steady-state polarization curves (Fig. S7a†) show that all the FNT-MEAs exhibit higher performance than the CCM-MEA under the same catalyst loading, confirming the superiority of the 3D-FNT structure in promoting the electrolysis performance. As for FNT-MEAs, with the decrease in the I/C ratio, the performance gradually increases until the I/C ratio reaches 6%. The FNT-MEA-Nafion 6 wt%-0.3 displays the best performance with the lowest cell voltage (1.711 V@1.5 A cm^{-2}). Interestingly, the FNT-MEA without the addition of the Nafion resin also shows encouraging performance, implying that the pure PEO nanofiber has the capacity for proton conduction. The above analysis confirms that the Nafion resin content in ACL will significantly influence the MEA performance and the optimal I/C ratio is 6%.

The MEA with a lower IrO_2 loading of 0.1 mg cm^{-2} (FNT-MEA-0.1) is also prepared. Strikingly, the performance only shows a slight decline compared to that of the FNT-MEA-Nafion 6 wt%-0.3 and the cell voltage achieves 1.737 V at a current density of 1.5 A cm^{-2} (Fig. 3a). In contrast, the cell voltage (1.874 V@1.5 A cm^{-2}) of CCM-MEA-0.1 is much higher than that of FNT-MEA-0.1. Noteworthily, the performance of FNT-MEA-0.1 is even higher than that of the CCM-MEA with 10-fold IrO_2 loading (1.740 V@1.5 A cm^{-2}), demonstrating the positive effectiveness of the 3D-FNT structure in improving the IrO_2 utilization efficiency. Fig. 3b shows the Tafel plots of the three kinds of MEAs, which are obtained from the corresponding *iR*-corrected polarization curves (Fig. S9†). The Tafel slope for FNT-MEA-0.1 is 53.3 mV dec^{-1}, lower than that of CCM-MEA-0.1, indicative of the fast OER kinetics for the catalyst within the 3D-FNT structure. Electrochemical active areas (ECSAs) of the CCM-MEAs and FNT-MEA were calculated from double-layer capacitance (Fig. S10† and 3c) at non-Faraday potential windows from 0.86 to 0.96 V *versus* the dynamic hydrogen electrode (*vs.* DHE). The ECSA of FNT-MEA-0.1 is 431.7 m^2 $g_{IrO_2}^{-1}$, which is 3.4 and 1.4 times higher than that of CCM-MEA-1 (127.2 m^2 $g_{IrO_2}^{-1}$) and CCM-MEA-0.1 (298.3 m^2 $g_{IrO_2}^{-1}$), respectively (Fig. 3d), revealing the highly exposed active sites for the 3D-FNT structure. Moreover, the IrO_2 utilization efficiency in MEAs was also calculated by obtaining the relative values of the ECSA measured in the MEA to the ECSA measured in the RDE.[31] The result (Fig. 3d) shows that FNT-MEA-0.1 exhibits the highest utilization efficiency of IrO_2 (96.4%) in the ACL, which is much higher than that of CCM-MEA-1 and CCM-MEA-0.1 with values of 28.4 and 66.6%, respectively. The polarization curves normalized to the mass of Ir (Fig. 3e) and the corresponding mass normalized activities (Fig. S11†) demonstrate that the FNT-MEA exhibits much higher mass activity than CCM-MEAs at various potentials. Significantly, the mass activity of such a 3D-FNT-MEA with ultralow IrO_2 loading exceeds that of the most reported PEMWE electrolyzers, again confirming the advancement of the 3D-FNT structure (Fig. 3f and Table S2†).[19,23,32–38]

To deeply reveal the promotion mechanism of the 3D-FNT structure, electrochemical impedance spectroscopy (EIS) spectra were comprehensively analyzed. Fig. S12† shows the

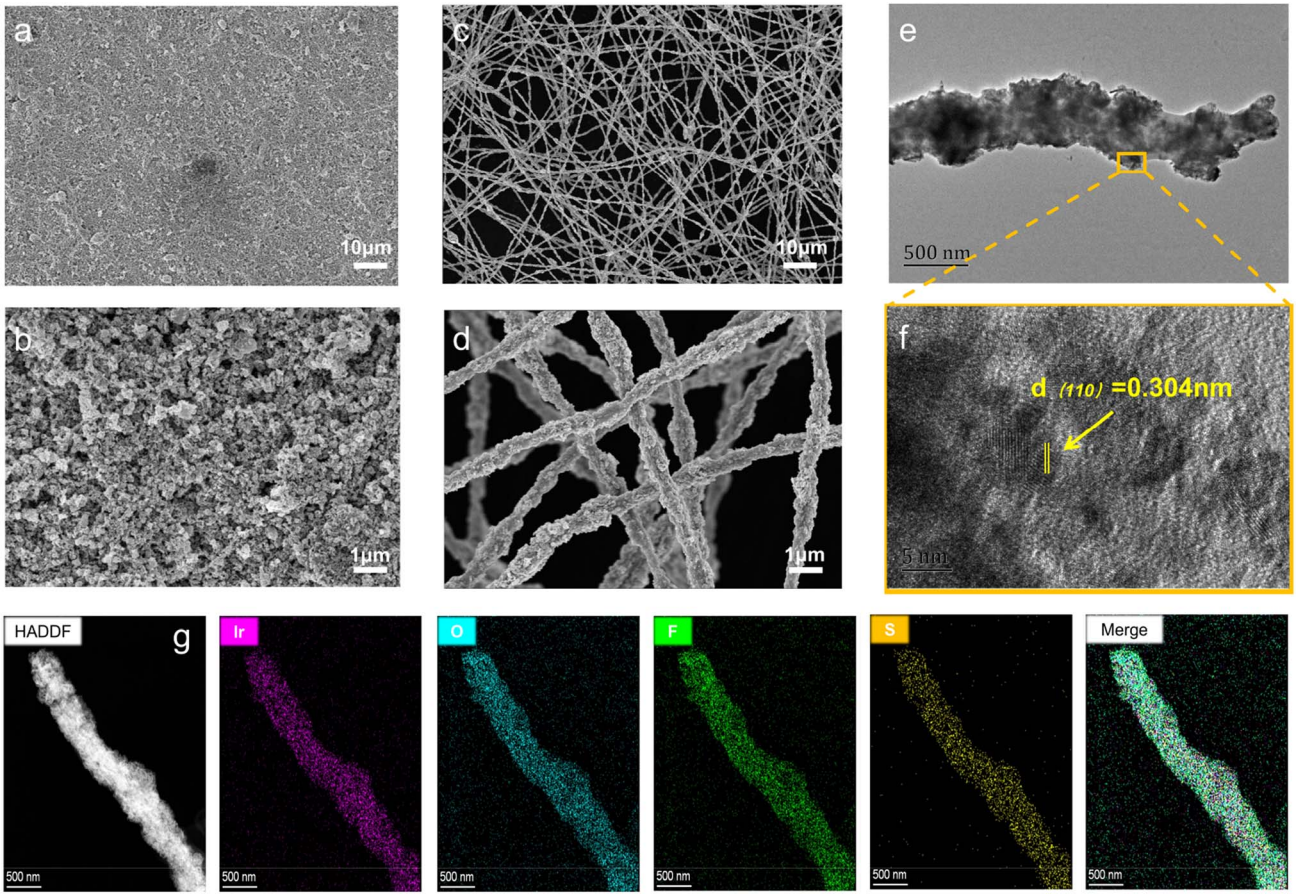

Fig. 2 (a) The SEM image of the tightly packed structure for a CCM anode and (b) corresponding enlarged image. (c) The SEM image of the 3D nanofiber network anode and (d) the corresponding enlarged image. (e) The TEM and (f) HRTEM images of the single nanofiber. (g) The EDS-mapping for the single nanofiber.

Nyquist plots of CCM-MEA-0.1 and FNT-MEA-0.1 operated at a potential of 1.3−1.5 V. The semicircle of FNT-MEA-0.1 is obviously smaller than that of CCM-MEA-0.1 at the same potential, attesting to the low charge transfer resistance (R_{ct}) of the novel MEA, which is consistent with the Tafel results. Moreover, the semicircle decreases as the potential increases from 1.3 to 1.5 V, because R_{ct} is inversely proportional to the current density. Fig. 4a shows the Nyquist plots of the CCM-MEAs and the FNT-MEA at an applied potential of 1.6 V (the inset shows an equivalent circuit model). The fitted parameters are summarized in Table S1.† As shown in Fig. 4b, the fitted R_{ct} value of FNT-MEA-0.1 is 36% lower than that of CCM-MEA-0.1. Meanwhile, the ohmic resistance (R_s) of the FNT-MEA is also lower than that of CCM-MEA, which is probably attributed to the improved interface contact between 3D-FNT and PEM. Of note, at a potential of 1.6 V, the Warburg impedance appears in the low-frequency region, demonstrating the appearance of mass-transfer polarization. As shown in eqn (1), the diffusion coefficient (D) is inversely related to the Weber coefficient (σ) in electrochemical impedance and the σ can be calculated from Fig. 4c. We can thus quantify the mass-transfer of different MEAs at high potential. Accordingly, the D ofFNT-MEA-0.1 is 1.34 times higher than that of CCM-MEA-0.1, definitely verifying that the unique 3D-FNT structure greatly improves the mass transport in the ACL. Beyond this, the wettability properties of the MEA also play an essential role in promoting the performance of PEMWE at high current density through accelerating the water transport. As shown in Fig. S13a,† CCM-MEA-0.1 exhibits a contact angle as high as 143°, which is unfavorable for water transport. In contrast, the contact angle of FNT-MEA-0.1 (Fig. S13b†) is reduced to 113°, indicating that the novel 3D-FNT structure contributes to the improvement hydrophilicity, which expedites water transportation during the electrolysis.

$$D = \frac{R^2T^2}{2A^2n^4F^4C^2\sigma^2} \quad (1)$$

The proton-transfer within the ACL is also crucial for the performance improvement of the MEA, but it is always neglected. Here we performed EIS under the N_2 (anode)/H_2 (cathode) conditions using the previously reported one-dimensional transmission-line model (TLM) to accurately quantify the proton conductivity[28] within the ACL. As shown in Fig. S14,† the ACL is modeled using various elements, including proton conduction resistance (R_{H^+}), charge transfer resistance (R_{ct}), and the double-layer capacitance (C_{dl}).

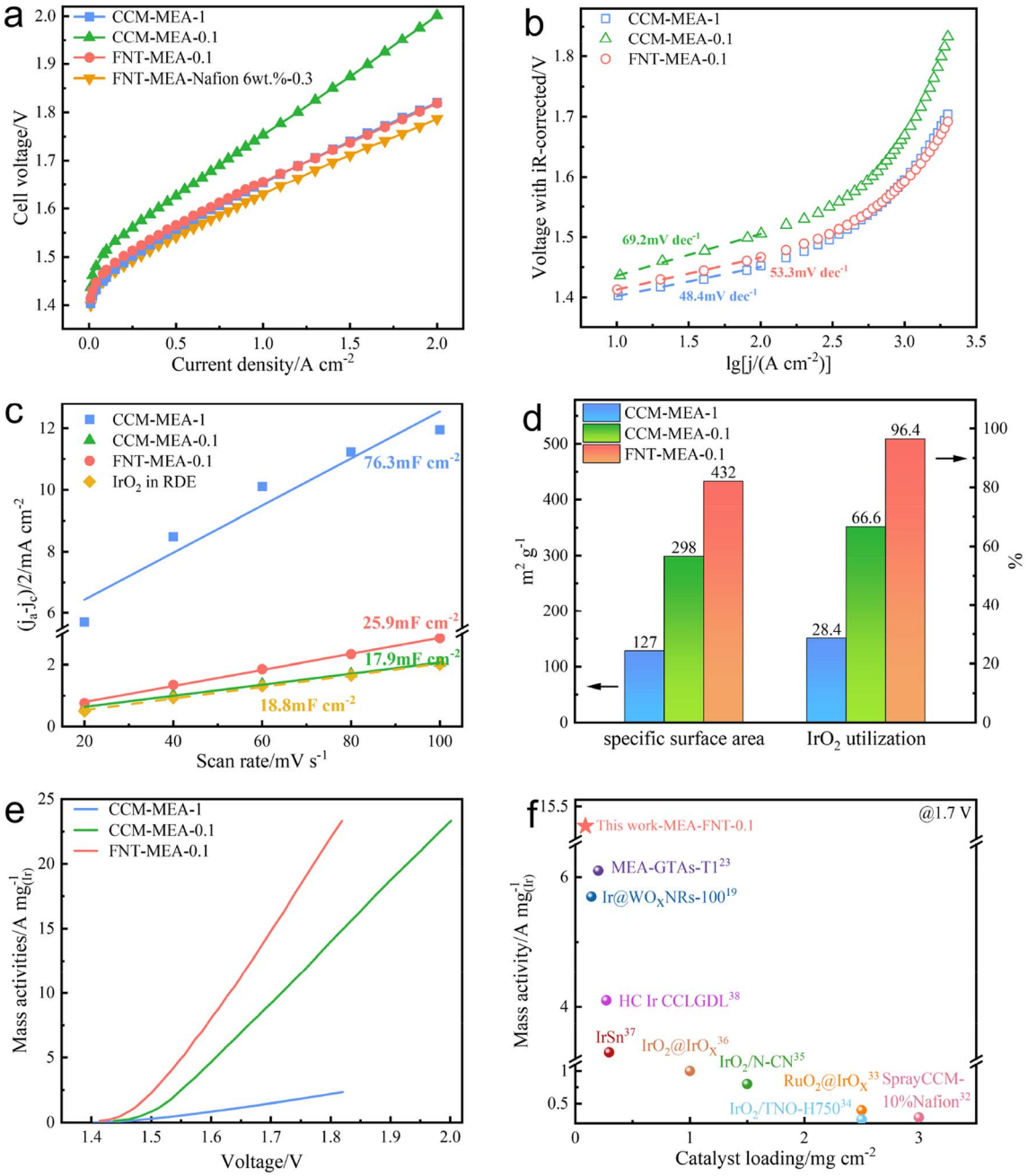

Fig. 3 (a) Steady-state polarization curves of the MEAs with different catalyst loading operations at 80 °C. (b) Tafel plots for the CCM-MEAs and FNT-MEA. (c) The double-layer capacitance calculated in MEAs and RDE configurations. (d) The estimated ECSAs and catalyst utilization of the CCM-MEAs and FNT-MEA. (e) The mass normalized polarization curves of CCM-MEAs and the FNT-MEA. (f) The comparison of mass activity@1.7 V of the FNT-MEA with that of other reported MEA structures.

Assuming a uniform potential distribution in the ACL, the $R_{H^+}/3$ can be obtained through low-frequency capacitance extrapolated to the real axis, as shown in Fig. 4d. The obtained $R_{H^+}/3$ for MEA-FNT-0.1 is 2.9 Ω cm^{-2}, which is *ca.* 2.8- and 7.8-fold smaller than those of CCM-MEA-1 (8.1 Ω cm^{-2}) and CCM-MEA-0.1 (22.5 Ω cm^{-2}) respectively, directly corroborating that the continuous 1D Nafion nanofiber channels dramatically facilitate the proton-transfer within the ACL, which might be a primary reason for the performance enhancement for the FNT-MEA. To further understand the contribution of Nafion nanofiber channels, the proton conduction resistances of FNT-MEAs with different I/C ratios were evaluated. As shown in Fig. S7b and c,† the proton conduction resistances for all the FNT-MEAs are obviously lower than that of CCM-MEA, indicative of the positive effectiveness of the 1D Nafion channel on the promotion of proton conduction. In particular, the proton conduction resistance for the FNT-MEA exhibits a volcano-

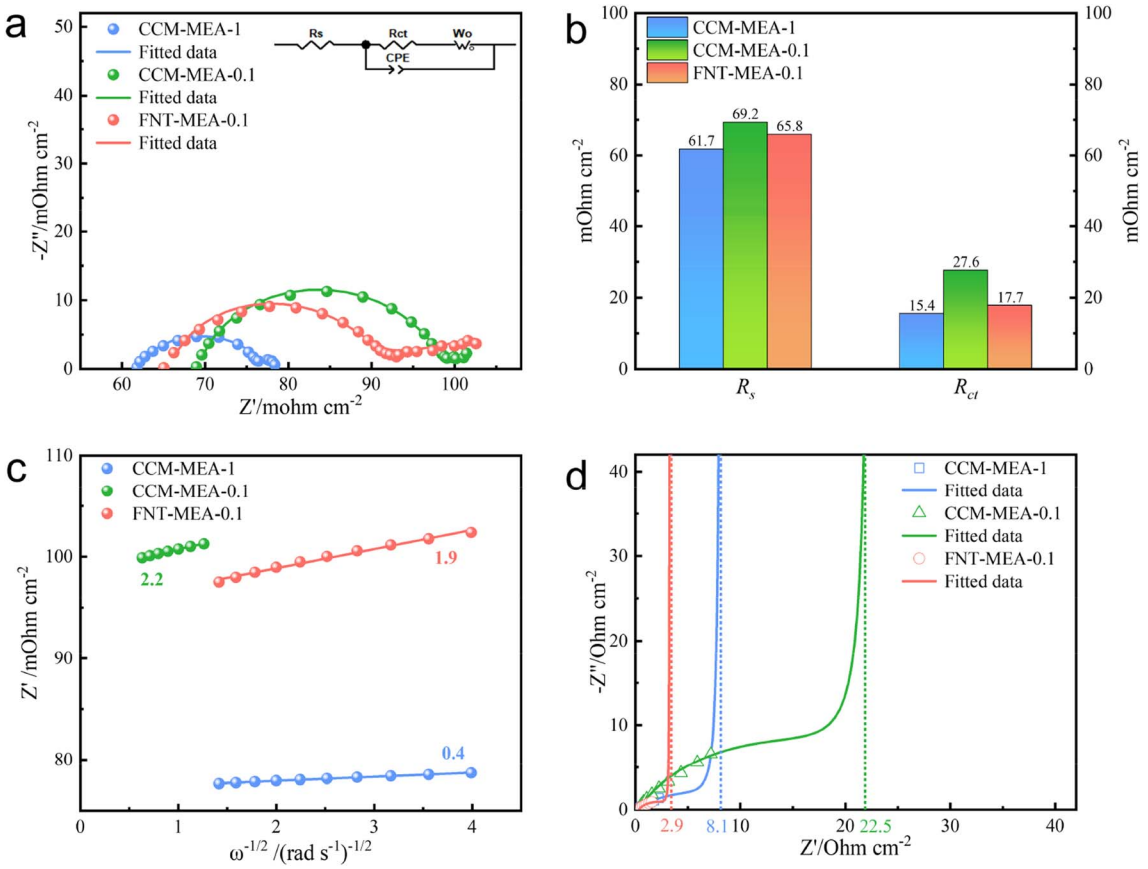

Fig. 4 (a) Nyquist plots of the CCM-MEAs and FNT-MEA at 1.6 V *vs.* DHE. The inset shows an equivalent circuit. (b) The ohmic resistance (R_s) and charge transfer resistance (R_{ct}) of the CCM-MEAs and FNT-MEA. (c) Weber coefficient of the CCM-MEAs and FNT-MEA, which can reflect mass transfer at high potential. (d) Nyquist plots of the ACL for CCM-MEAs and FNT-MEA under H_2/N_2 conditions.

type trend that depends on the I/C ratio and reaches the lowest value when the I/C ratio is 6%, which also corresponds to the best electrolysis performance.

The long-term stability test was conducted at a constant current density of 1 A cm^{-2} to verify the practical application potential of this novel FNT-MEA. The stability of CCM-MEAs

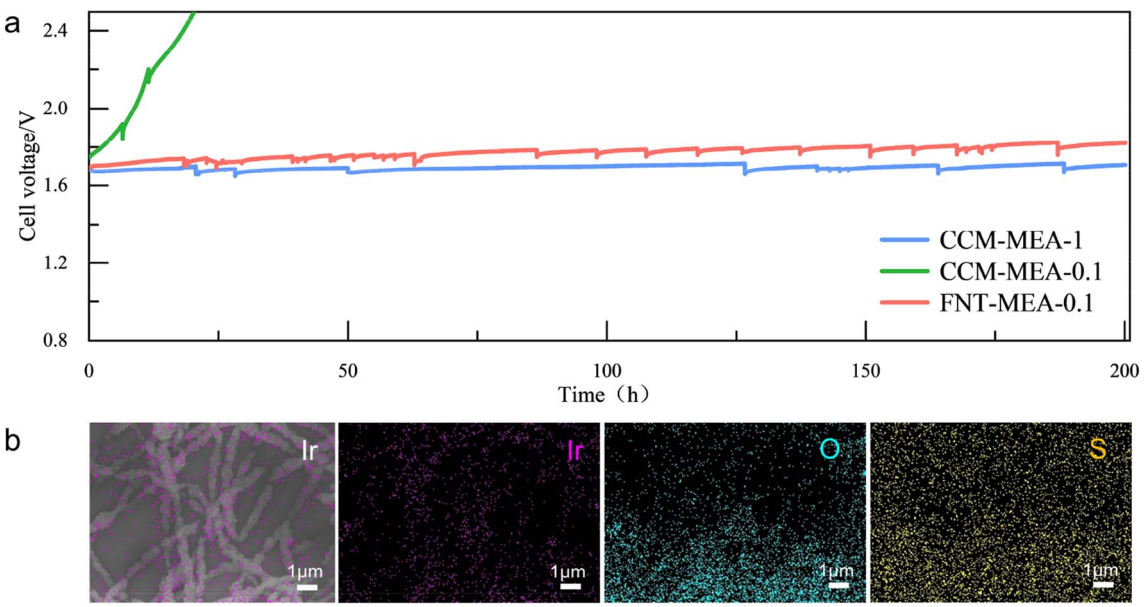

Fig. 5 (a) The stability test of the CCM-MEAs and FNT-MEA at 1 A cm^{-2} and 65 °C. (b) The corresponding EDS-mapping after the durability test.

was also evaluated as a comparison. As depicted in Fig. 5a, FNT-MEA-0.1 exhibits satisfactory stability with a voltage decay of 7.5% for more than 200 h, which is even comparable to that of the CCM-MEA with 10-fold IrO_2 loading (1.0 mg cm^{-2}). In contrast, the cell voltage of the CCM-MEA with the same low IrO_2 loading (0.1 mg cm^{-2}) rapidly increases to 2.5 V within 20 h, indicative of the inferior structural stability. Fig. 5b shows that the 3D-FNT structure is well-preserved after a long-term stability test. The EDS-mapping also demonstrates the existence of Ir, O, and S elements, which are homogeneously dispersed on the nanofiber.

3 Conclusion

In summary, the novel MEA with a 3D-FNT structure is a controllable construction through electrospinning and nanotransfer techniques. The unique nanofiber networks not only expedite water/oxygen transport at high current density due to high porosity, but also promoteproton-conduction within the ACL owing to the 1D Nafion–PEO nanofiber. As a result, the 3D-FNT-MEA with an ultralow IrO_2 loading (0.1 mg cm^{-2}) delivers an encouraging performance with a cell voltage of 1.737 V@1.5 A cm^{-2}, which is far lower than that of the traditional CCM-MEA (1.874 V@1.5 A cm^{-2}) with the same IrO_2 loading and even higher than that of the CCM-MEA with 10-fold IrO_2 loading (1.740 V@1.5 A cm^{-2}), realizing the large reduction of Ir usage in PEMWE. This work offers an ideal route to maximize the TPRB and to boost the performance of MEAs, suggesting practical application potential in PEMWE.

Data availability

The data that support the findings of this study are available from the corresponding author upon reasonable request.

Author contributions

Maolin Geng: investigation, formal analysis, validation, writing – original draft. Zhenlan Dou: supervision. Hao Zhao: investigation. Qiansen Wang: investigation. Chunyan Zhang: investigation. Zhiqing Zou: conceptualization. Jun Li: methodology. Hui Yang: supervision, project administration. Qingqing Cheng: conceptualization, methodology, funding acquisition, writing – review & editing.

Conflicts of interest

The authors declare no conflict of interest.

Acknowledgements

This work was supported by the National Key R&D Program of China (2021YFB4000200), the National Natural Science Foundation of China (No. 22002184), the Shanghai Science and Technology Innovation Action Plan (23ZR1471000 and 20dz1205400) and the State Grid Shanghai Municipal Electric Power Company.

References

1 S. Yuan, C. F. Zhao, X. Y. Cai, L. An, S. Y. Shen, X. H. Yan and J. L. Zhang, *Prog. Energy Combust. Sci.*, 2023, **96**, 101075.
2 S. M. Ahn, J. E. Park, G. Y. Jang, H. Y. Jeong, D. M. Yu, J. K. Jang, J. C. Lee, Y. H. Cho and T. H. Kim, *ACS Energy Lett.*, 2022, **7**, 4427–4435.
3 J. D. Gong, C. Sun, H. A. Shi and W. Y. Tan, *Int. J. Hydrog. Energy*, 2023, **48**, 30642–30652.
4 Z. P. Shi, J. Li, Y. B. Wang, S. W. Liu, J. B. Zhu, J. H. Yang, X. Wang, J. Ni, Z. Jiang, L. J. Zhang, Y. Wang, C. P. Liu, W. Xing and J. J. Ge, *Nat. Commun.*, 2023, **14**, 843.
5 F. Liao, K. Yin, Y. J. Ji, W. X. Zhu, Z. L. Fan, Y. Y. Li, J. Zhong, M. W. Shao, Z. H. Kang and Q. Shao, *Nat. Commun.*, 2023, **14**, 1248.
6 H. Ashassi-Sorkhabi, A. Kazempour, S. Moradi-Alavian, E. Asghari and J. J. Lamb, *Int. J. Hydrog. Energy*, 2023, **48**, 29865–29876.
7 H. C. Ma, X. Huang, L. Y. Li, W. Peng, S. Lin, Y. Ding and L. Q. Mai, *Small*, 2023, **19**, 2302685.
8 H. T. B. Ngoc, L. Dohyeon, K. Soo-Kil, K. M. Jun and K. O. Joong, *J. Mater. Chem. A*, 2023, **11**, 14221–14231.
9 H. Huang, H. Kim, A. Lee, S. Kim, W. G. Lim, C. Y. Park, S. Kim, S. K. Kim and J. Lee, *Nano Energy*, 2021, **88**, 106276.
10 J. Qi, H. Y. Zeng, L. Gu, Z. F. Liu, Y. Q. Zeng, E. N. Hong, Y. C. Lai, T. H. Liu and C. Z. Yang, *ACS Appl. Mater. Interfaces*, 2023, **15**, 15269–15278.
11 M. S. Wilson, J. A. Valerio and S. Gottesfeld, *Electrochim. Acta*, 1995, **40**, 355–363.
12 H. L. Tang, S. L. Wang, M. Pan, S. P. Jiang and Y. Z. Ruan, *Electrochim. Acta*, 2007, **52**, 3714–3718.
13 Y. G. Chun, C. S. Kim, D. H. Peck and D. R. Shin, *J. Power Sources*, 1998, **71**, 174–178.
14 Q. Q. Cheng, Y. L. Wang, J. J. Jiang, Z. Q. Zou, Y. Zhou, J. H. Fang and H. Yang, *J. Mater. Chem. A*, 2015, **3**, 15177–15183.
15 C. Y. Chen and C. S. Tsao, *Int. J. Hydrog. Energy*, 2006, **31**, 391–398.
16 J. S. Chai, Y. Zhou, J. Fan, J. J. Jiang, T. Yuan, H. F. Zhang, Z. Q. Zou, H. D. Qian and H. Yang, *Int. J. Hydrog. Energy*, 2015, **40**, 6647–6654.
17 Q. H. Huang, J. J. Jiang, J. S. Chai, T. Yuan, H. F. Zhang, Z. Q. Zou, X. G. Zhang and H. Yang, *J. Power Sources*, 2014, **262**, 213–218.
18 L. Wan, Z. Xu, Q. Xu, P. C. Wang and B. G. Wang, *Energy Environ. Sci.*, 2022, **15**, 1882–1892.
19 G. Jiang, H. Yu, Y. Li, D. Yao and Z. Shao, *ACS Appl. Mater. Interfaces*, 2021, **13**, 15073–15082.
20 C. Lee, W. J. M. Kort-Kamp, H. R. Yu, D. A. Cullen, B. M. Patterson, T. A. Arman, S. K. Babu, R. Mukundan, R. L. Borup and J. S. Spendelow, *Nat. Energy*, 2023, **8**, 685–694.
21 Y. C. Zeng, X. Q. Guo, Z. G. Shao, H. M. Yu, W. Song, Z. Q. Wang, H. J. Zhang and B. L. Yi, *J. Power Sources*, 2017, **342**, 947–955.

22 J. E. Park, S. Kim, O. H. Kim, C. Y. Ahn, M. J. Kim, S. Y. Kang, T. I. Jeon, J. G. Shim, D. W. Lee, J. H. Lee, Y. H. Cho and Y. E. Sung, *Nano Energy*, 2019, **58**, 158–166.
23 S. Dong, C. Y. Zhang, Z. Y. Yue, F. R. Zhang, H. Zhao, Q. Q. Cheng, G. L. Wang, J. F. Xu, C. Chen, Z. Q. Zou, Z. L. Dou and H. Yang, *Nano Lett.*, 2022, **22**, 9434–9440.
24 U. Babic, T. J. Schmidt and L. Gubler, *J. Electrochem. Soc.*, 2018, **165**, J3016–J3018.
25 R. Makharia, M. F. Mathias and D. R. Baker, *J. Electrochem. Soc.*, 2005, **152**, A970–A977.
26 M. C. Lefebvre, R. B. Martin and P. G. Pickup, *Electrochem. Solid-State Lett.*, 1999, **2**, 259–261.
27 C. Y. Chen, P. Yang, Y. S. Lee and K. F. Lin, *J. Power Sources*, 2005, **141**, 24–29.
28 U. Babic, E. Nilsson, A. Patru, T. J. Schmidt and L. Gubler, *J. Electrochem. Soc.*, 2019, **166**, F214–F220.
29 S. Wang, G. Sun, Z. Wu and Q. Xin, *J. Power Sources*, 2007, **165**, 128–133.
30 Y. Sheikhnejad and S. A. G. Nassab, *Renew. Energy*, 2021, **169**, 437–450.
31 Q. Gong, H. Zhang, H. R. Yu, S. Jeon, Y. Ren, Z. Z. Yang, C. J. Sun, E. A. Stach, A. C. Foucher, Y. K. Yu, M. Smart, G. M. Filippelli, D. A. Cullen, P. Liu and J. Xie, *Matter*, 2023, **6**, 963–982.
32 Z. Q. Xie, S. L. Yu, G. Q. Yang, K. Li, L. Ding, W. T. Wang and F. Y. Zhang, *Int. J. Hydrog. Energy*, 2021, **46**, 1155–1162.
33 H. Lv, S. Wang, J. K. Li, C. F. Shao, W. Zhou, X. J. Shen, M. Z. Xue and C. M. Zhang, *Appl. Surf. Sci.*, 2020, **514**, 145943.
34 H. Lv, S. Wang, C. P. Hao, W. Zhou, J. K. Li, M. Z. Xue and C. M. Zhang, *ChemCatChem*, 2019, **11**, 2511–2519.
35 S. Wang, H. Lv, F. M. Tang, Y. W. Sun, W. X. Ji, W. Zhou, X. J. Shen and C. M. Zhang, *Chem. Eng. J.*, 2021, **419**, 129455.
36 C. Baik, S. W. Lee and C. Pak, *Electrochim. Acta*, 2021, **390**, 138885.
37 G. Jiang, H. M. Yu, J. K. Hao, J. Chi, Z. X. Fan, D. W. Yao, B. W. Qin and Z. G. Shao, *J. Energy Chem.*, 2019, **39**, 23–28.
38 L. Ding, W. T. Wang, Z. Q. Xie, K. Li, S. L. Yu, C. B. Capuano, A. Keane, K. Ayers and F. Y. Zhang, *ACS Appl. Mater. Interfaces*, 2023, **15**, 24284–24295.